Measurement of *CP* asymmetries in $B^0 \to K^0_S K^0_S K^0_S$ decays at Belle II

I. Adachi, L. Aggarwal, H. Ahmed, H. Aihara, N. Akopov, A. Aloisio, N. Anh Ky, D. M. Asner, H. Atmacan, T. Aushev, V. Aushev, M. Aversano, R. Ayad, V. Babu, H. Bae, S. Bahinipati, P. Bambade, Sw. Banerjee, S. Bansal, M. Barrett, J. Baudot, M. Bauer, A. Baur, A. Beaubien, F. Becherer, J. Becker, P. K. Behera, J. V. Bennett, F. U. Bernlochner, V. Bertacchi, M. Bertemes, E. Bertholet, M. Bessner, S. Bettarini, B. Bhuyan, F. Bianchi, L. Bierwirth, T. Bilka, D. Biswas, A. Bobrov, D. Bodrov, A. Bolz, A. Bondar, J. Borah, A. Bozek, M. Bračko, P. Branchini, R. A. Briere, T. E. Browder, A. Budano, S. Bussino, M. Campajola, L. Cao, G. Casarosa, C. Cecchi, J. Cerasoli, M.-C. Chang, P. Chang, R. Cheaib, P. Cheema, V. Chekelian, C. Chen, B. G. Cheon, K. Chilikin, K. Chirapatpimol, H.-E. Cho, K. Cho, S.-J. Cho, S.-K. Choi, S. Choudhury, J. Cochran, L. Corona, L. M. Cremaldi, S. Das, F. Dattola, E. De La Cruz-Burelo, S. A. De La Motte, G. De Nardo, M. De Nuccio, G. De Pietro, R. de Sangro, M. Destefanis, S. Dey, A. De Yta-Hernandez, R. Dhamija, A. Di Canto, F. Di Capua, J. Dingfelder, Z. Doležal, I. Domínguez Jiménez, T. V. Dong, M. Dorigo, K. Dort, D. Dossett, S. Dreyer, S. Dubey, G. Dujany, P. Ecker, M. Eliachevitch, D. Epifanov, P. Feichtinger, T. Ferber, D. Ferlewicz, T. Fillinger, C. Finck, G. Finocchiaro, A. Fodor, F. Forti, A. Frey, B. G. Fulsom, A. Gabrielli, E. Ganiev, M. Garcia-Hernandez, R. Garg, A. Garmash, G. Gaudino, V. Gaur, A. Gaz, A. Gellrich, G. Ghevondyan, D. Ghosh, H. Ghumaryan, G. Giakoustidis, R. Giordano, A. Giri, A. Glazov, B. Gobbo, R. Godang, O. Gogota, P. Goldenzweig, W. Gradl, T. Grammatico, S. Granderath, E. Graziani, D. Greenwald, Z. Gruberová, T. Gu, Y. Guan, K. Gudkova, S. Halder, Y. Han, K. Hara, T. Hara, K. Hayasaka, H. Hayashii, S. Hazra, C. Hearty, M. T. Hedges, A. Heidelbach, I. Heredia de la Cruz, M. Hernández Villanueva, A. Hershenhorn, T. Higuchi, E. C. Hill, M. Hoek, M. Hohmann, P. Horak, C.-L. Hsu, T. Humair, T. Iijima, K. Inami, N. Ipsita, A. Ishikawa, S. Ito, R. Itoh, M. Iwasaki, P. Jackson, W. W. Jacobs, D. E. Jaffe, E.-J. Jang, Q. P. Ji, S. Jia, Y. Jin, A. Johnson, K. K. Joo, H. Junkerkalefeld, H. Kakuno, M. Kaleta, D. Kalita, A. B. Kaliyar, J. Kandra, K. H. Kang, S. Kang, G. Karyan, T. Kawasaki, F. Keil, C. Ketter, C. Kiesling, C.-H. Kim, D. Y. Kim, K.-H. Kim, Y.-K. Kim, H. Kindo, K. Kinoshita, P. Kodyš, T. Koga, S. Kohani, K. Kojima, T. Konno, A. Korobov, S. Korpar, E. Kovalenko, R. Kowalewski, T. M. G. Kraetzschmar, P. Križan, P. Krokovny, Y. Kulii, T. Kuhr, J. Kumar, M. Kumar, R. Kumar, K. Kumara, T. Kunigo, A. Kuzmin, Y.-J. Kwon, S. Lacaprara, Y.-T. Lai, T. Lam, L. Lanceri, J. S. Lange, M. Laurenza, K. Lautenbach, R. Leboucher, F. R. Le Diberder, P. Leitl, D. Levit, C. Li, L. K. Li, Y. Li, J. Libby, Q. Y. Liu, Z. Q. Liu, D. Liventsev, S. Longo, A. Lozar, T. Lueck, C. Lyu, Y. Ma, M. Maggiora, S. P. Maharana, R. Maiti, S. Maity, G. Mancinelli, R. Manfredi, E. Manoni, M. Mantovano, D. Marcantonio, S. Marcello, C. Marinas, L. Martel, C. Martellini, A. Martini, T. Martinov, L. Massaccesi, M. Masuda, T. Matsuda, D. Matvienko, S. K. Maurya, J. A. McKenna, R. Mehta, F. Meier, M. Merola, F. Metzner, M. Milesi, C. Miller, M. Mirra, K. Miyabayashi, H. Miyake, R. Mizuk, G. B. Mohanty, N. Molina-Gonzalez, S. Mondal, S. Moneta, H.-G. Moser, M. Mrvar, R. Mussa, I. Nakamura, K. R. Nakamura, M. Nakao, Y. Nakazawa, A. Narimani Charan, M. Naruki, Z. Natkaniec, A. Natochii, L. Nayak, M. Nayak, G. Nazaryan, M. Neu, C. Niebuhr, N. K. Nisar, S. Nishida, S. Ogawa, Y. Onishchuk, H. Ono, Y. Onuki, P. Oskin, F. Otani, P. Pakhlov, G. Pakhlova, A. Paladino, A. Panta, E. Paoloni, S. Pardi, K. Parham, H. Park, S.-H. Park, B. Paschen, A. Passeri, S. Patra, S. Paul, T. K. Pedlar, I. Peruzzi, R. Peschke, R. Pestotnik, F. Pham, M. Piccolo, L. E. Piilonen, G. Pinna Angioni, P. L. M. Podesta-Lerma, T. Podobnik, S. Pokharel, C. Praz, S. Prell, E. Prencipe, M. T. Prim, H. Purwar, N. Rad, P. Rados, G. Raeuber, S. Raiz, N. Rauls, M. Reif, S. Reiter, M. Remnev, I. Ripp-Baudot, G. Rizzo, L. B. Rizzuto, S. H. Robertson, M. Roehrken, J. M. Roney, A. Rostomyan, N. Rout, G. Russo, D. Sahoo, D. A. Sanders, S. Sandilya, A. Sangal, L. Santelj, Y. Sato, V. Savinov, B. Scavino, C. Schmitt, C. Schwanda, A. J. Schwartz, Y. Seino, A. Selce, K. Senyo, J. Serrano, M. E. Sevior, C. Sfienti, W. Shan, C. Sharma, X. D. Shi, T. Shillington, T. Shimasaki, J.-G. Shiu, D. Shtol, B. Shwartz, A. Sibidanov, F. Simon, J. B. Singh, J. Skorupa, R. J. Sobie, M. Sobotzik, A. Soffer, A. Sokolov, E. Solovieva, S. Spataro, B. Spruck, M. Starič, P. Stavroulakis, S. Stefkova, Z. S. Stottler, R. Stroili, J. Strube, Y. Sue, M. Sumihama, K. Sumisawa, W. Sutcliffe, H. Svidras, M. Takahashi, M. Takizawa, U. Tamponi, K. Tanida, H. Tanigawa, F. Tenchini, A. Thaller, O. Tittel, R. Tiwary, D. Tonelli, E. Torassa, N. Toutounji, K. Trabelsi, I. Tsaklidis, M. Uchida, I. Ueda, Y. Uematsu, T. Uglov, K. Unger, Y. Unno, K. Uno, S. Uno, P. Urquijo, Y. Ushiroda, S. E. Vahsen, R. van Tonder, G. S. Varner, K. E. Varvell, M. Veronesi,

V. S. Vismaya, L. Vitale, V. Vobbilisetti, R. Volpe, B. Wach, M. Wakai, S. Wallner, E. Wang, M.-Z. Wang, X. L. Wang, Z. Wang, A. Warburton, M. Watanabe, S. Watanuki, M. Welsch, C. Wessel, X. P. Xu, B. D. Yabsley, S. Yamada, W. Yan, S. B. Yang, J. Yelton, J. H. Yin, K. Yoshihara, C. Z. Yuan, Y. Yusa, L. Zani, Y. Zhang, V. Zhilich, J. S. Zhou, Q. D. Zhou, X. Y. Zhou, and V. I. Zhukova

(Belle II Collaboration)

(Received 7 March 2024; accepted 17 May 2024; published 27 June 2024)

We report a measurement of decay-time-dependent charge-parity (CP) asymmetries in $B^0 \to K^0_S K^0_S K^0_S$ decays. We use 387×10^6 $B\bar{B}$ pairs collected at the $\Upsilon(4S)$ resonance with the Belle II detector at the SuperKEKB asymmetric-energy electron-positron collider. We reconstruct 220 signal events and extract the CP-violating parameters S and C from a fit to the distribution of the decay-time difference between the two B mesons. The resulting confidence region is consistent with previous measurements in $B^0 \to K^0_S K^0_S K^0_S$ and $B^0 \to (c\bar{c})K^0$ decays and with predictions based on the standard model.

DOI: 10.1103/PhysRevD.109.112020

I. INTRODUCTION

In the standard model (SM), the charmless three-body decay $B^0 \to K^0_S K^0_S K^0_S$ is mediated by the $b \to sq\bar{q}$ quark transition, which is dominated by a one-loop process, the so-called penguin amplitude. Charge-conjugate decays are implied hereafter unless specified otherwise. Penguin amplitudes are suppressed in the SM, e.g., $\mathcal{B}(B^0 \to K^0_S K^0_S K^0_S) = (6.0 \pm 0.5) \times 10^{-6}$ [1] and imply exchanges of virtual particles where SM particles can be replaced by a broad class of non-SM particles. These features make these decays sensitive to possible contributions from non-SM physics [2]. A key probe of such contributions is provided by decay-time-dependent CP-violating asymmetries of the B^0 and $\bar{B}^0$ decay rates. These asymmetries arise from interference between amplitudes for direct decay and decay following flavor oscillations, due to the irreducible phase in the Cabibbo-Kobayashi-Maskawa (CKM) quark-mixing matrix [3]. Precise measurements of these asymmetries using $B^0\bar{B}^0$ pairs are a primary goal of experiments in electron-positron collisions at the $\Upsilon(4S)$ resonance. If one of the neutral B mesons, B_{CP}, decays into a CP eigenstate f_{CP} at proper time t_{CP} and the other, $B_{\rm tag}$, decays into a flavor-specific final state $f_{\rm tag}$ at proper time $t_{\rm tag}$, the probability density for observing a $B_{\rm tag}$ with flavor q_f at $\Delta t \equiv t_{CP} - t_{\rm tag}$ is [4–6]

$$\mathcal{P}(\Delta t, q_f) = \frac{e^{-|\Delta t|/\tau_{B^0}}}{4\tau_{B^0}}(1 + q_f[S\sin(\Delta m_d \Delta t) - C\cos(\Delta m_d \Delta t)]), \quad (1)$$

where the flavor q_f is $+1(-1)$ for $B_{\rm tag} = B^0(\bar{B}^0)$, τ_{B^0} is the B^0 lifetime, Δm_d is the mass difference between the two mass eigenstates of the B^0-$\bar{B}^0$ system, and the CP asymmetries S and C express mixing-induced and direct CP violation, respectively [7]. The SM predicts that $S = -\sin 2\phi_1 - 0.02$ and $C = -0.007$ for decays into the CP-even final state $K^0_S K^0_S K^0_S$ [8]. The mixing phase $\phi_1 \equiv \arg[-V_{cd}V^*_{cb}/V_{td}V^*_{tb}]$ is a combination of CKM matrix elements. The uncertainty in the SM prediction for S is smaller than 0.01; hence, a large deviation in $B^0 \to K^0_S K^0_S K^0_S$ decays would indicate non-SM physics. The Belle [9] and *BABAR* [10] experiments reported these asymmetries with comparable uncertainties dominated by the sample size, yielding world-average values $S = -0.83 \pm 0.17$ and $C = -0.15 \pm 0.12$ [11]. While these agree with the SM predictions, the large uncertainties limit the sensitivity to non-SM sources. Additional measurements are needed.

We report a measurement of S and C in $B^0 \to K^0_S K^0_S K^0_S$ decays using electron-positron collisions at the $\Upsilon(4S)$ collected by the Belle II experiment. We reconstruct signal (B_{CP}) $B^0 \to K^0_S K^0_S K^0_S$ decays followed by $K^0_S \to \pi^+\pi^-$ decays and suppress background using two multivariate classifiers. We then measure q_f using the remaining charged particles in the event and Δt from the distance between the decay positions of B_{CP} and $B_{\rm tag}$. We divide the $B^0 \to K^0_S K^0_S K^0_S$ events into two classes based on the quality of the Δt information: time-differential events use Δt and determine S and C, while time-integrated events do not use Δt and contribute to the determination of C only. Fits to

signal-discriminating observables and decay time (when appropriate) determine the signal yield and *CP* asymmetries. We use the decay $B^+ \to K^0_S K^0_S K^+$ as a control channel to constrain the fit model from data.

II. THE BELLE II DETECTOR AND DATA SAMPLE

The Belle II experiment is located at SuperKEKB, which collides electrons and positrons at and near the $\Upsilon(4S)$ resonance [12]. The Belle II detector [13] has a cylindrical geometry and includes a six-layer silicon detector (VXD) and a 56-layer central drift chamber (CDC). These detectors reconstruct trajectories of charged particles (tracks). The VXD consists of two layers of silicon-pixel detectors (PXDs) surrounded by four layers of double-sided silicon-strip detectors [14]. Only the innermost PXD layer and one-sixth of the outermost layer are installed for the data analyzed here. The symmetry axis of these detectors, defined as the z axis, is almost coincident with the direction of the electron beam. Surrounding the CDC, which also provides $\mathrm{d}E/\mathrm{d}x$ energy-loss measurements, is a time-of-propagation counter [15] in the central region and an aerogel-based ring-imaging Cherenkov counter in the forward region. These detectors provide charged-particle identification. Surrounding them is an electromagnetic calorimeter based on CsI(Tl) crystals that primarily provides energy and timing measurements for photons and electrons. Outside of the calorimeter is a superconducting solenoid magnet. The magnet provides a 1.5 T magnetic field parallel to the z axis. Its flux return is instrumented with resistive-plate chambers and plastic-scintillator modules to detect muons, K^0_L mesons, and neutrons.

We use data collected at the $\Upsilon(4S)$ resonance in 2019–2022, corresponding to an integrated luminosity of (362 ± 2) fb^{-1} and containing $(387 \pm 6) \times 10^6$ $B\bar{B}$ pairs. We use simulated samples to train the multivariate classifiers and define fit models. The $e^+e^- \to \Upsilon(4S) \to B\bar{B}$ sample is generated using EvtGen [16] and PYTHIA [17]. In the simulated signal sample, one of the B mesons decays to the $B^0 \to K^0_S K^0_S K^0_S$ signal mode or the $B^+ \to K^0_S K^0_S K^+$ control mode according to phase space. The simulated $e^+e^- \to q\bar{q}$ sample, where q indicates an u, d, s, or c quark, is generated using the KKMC [18] generator interfaced with PYTHIA. We also use EvtGen to simulate the decay of short-lived particles. The detector response is simulated by GEANT4 [19]. Experimental and simulated data are analyzed with the Belle II software [20,21].

III. EVENT RECONSTRUCTION

The $\Upsilon(4S)$ is produced at the e^+e^- collision point with a Lorentz boost ($\beta\gamma$) of 0.288 and subsequently decays to a B and a $\bar{B}$ meson, which are both nearly at rest in the e^+e^- c.m. frame. Therefore, the B-meson pairs propagate nearly along the boost direction with known velocity in the laboratory. This allows one to approximate the difference between their decay times as $\Delta t = (z_{CP} - z_{\mathrm{tag}})/\beta\gamma c$, where $z_{CP(\mathrm{tag})}$ is the decay position of $B_{CP(\mathrm{tag})}$ projected onto the boost axis.

Events are selected online based on the number of charged particles and total energy deposited in the calorimeter with nearly 100% efficiency. Pairs of oppositely charged particles are used to reconstruct $K^0_S \to \pi^+\pi^-$ candidates. The four-momentum and decay vertex of the K^0_S candidate are obtained from a kinematic fit of the π^+ and π^- tracks. To reduce combinatorial background from incorrectly reconstructed K^0_S candidates, we use a boosted-decision-tree (BDT) classifier $O_{K^0_S}$ with 15 input variables that include the K^0_S flight length, the impact parameters of the K^0_S candidate and the $\pi^\pm$, and the number of measurement points (hits) in the VXD associated with the $\pi^\pm$. The most discriminating variables are the angle between the K^0_S momentum and the displacement of the K^0_S decay vertex from the beam interaction point (IP) and the K^0_S flight length normalized by its uncertainty. We select K^0_S candidates with invariant mass $M(\pi^+\pi^-)$ between 462.6 and 532.6 MeV/c^2, corresponding to about 35 units of the relevant resolution, and with an $O_{K^0_S}$ requirement that accepts 91% of K^0_S mesons. The mass window is wide since the BDT efficiently suppresses the background. These criteria are optimized as described later.

We reconstruct B_{CP} candidates by combining three K^0_S candidates and treat the particles not belonging to B_{CP} as B_{tag} decay products. We select B_{CP} candidates using the invariant mass $M(K^0_S K^0_S K^0_S)$ and the beam energy constrained mass $M_{\mathrm{bc}} \equiv \sqrt{E^2_{\mathrm{beam}} - |\vec{p}_B|^2 c^2}/c^2$, where E_{beam} and $\vec{p}_B$ are the beam energy and the momentum of the B meson in the e^+e^- c.m. frame. The difference between the beam energy and the energy of the B meson in the c.m. frame is not used unlike in previous analyses because of its correlation with M_{bc} [9,10]. We retain B_{CP} candidates satisfying $5.2 < M_{\mathrm{bc}} < 5.29$ and $5.08 < M(K^0_S K^0_S K^0_S) < 5.48$ GeV/c^2, but exclude those satisfying $5.265 < M_{\mathrm{bc}} < 5.29$ and $5.08 < M(K^0_S K^0_S K^0_S) < 5.2$ GeV/c^2 to avoid contamination by $B^{0(+)} \to K^0_S K^0_S K^{*0(+)}$ decays.

The dominant source of background is the $e^+e^- \to q\bar{q}$ continuum. We suppress this background by using another BDT classifier, O_{CS}, with the following input variables that exploit event topology: the cosine of the angle between the thrust axes of B_{CP} and B_{tag} in the e^+e^- c.m. frame, the magnitude of the B_{tag} thrust, the sum of the transverse momenta of the particles in the event, the squared four-momentum difference between the beams and the detected particles in the c.m. frame, and the modified Fox-Wolfram moments [22]. The B thrust axis is a unit vector $\hat{t}$ that maximizes the thrust magnitude $T \equiv (\sum_i |\hat{t} \cdot \vec{p}_i|)/(\sum_i |\vec{p}_i|)$, where $\vec{p}_i$ is the momentum of the B meson's ith decay product in the c.m. frame. The BDT classifier O_{CS} ranges from zero for backgroundlike events to one for

signal-like events. We use simulated events to train the classifier. A requirement of $O_{\rm CS} > 0.1$ results in 51% background rejection with a signal efficiency of 98%. We then calculate a transformation of the classifier, $O'_{\rm CS} = \log[(O_{\rm CS} - 0.1)/(1 - O_{\rm CS})]$, which yields a classifier distribution more convenient to parametrize. The selection criteria on K^0_S candidate mass and $O_{K^0_S}$ are determined by maximizing $N_{\rm sig}/\sqrt{N_{\rm sig} + N_{\rm bkg}}$, where $N_{\rm sig}$ and $N_{\rm bkg}$ are the expected yields of B_{CP} signal and background events determined from simulation, respectively, meeting the following signal-enhancement conditions: $5.27 < M_{\rm bc} < 5.29\ {\rm GeV}/c^2$, $5.18 < M(K^0_S K^0_S K^0_S) < 5.38\ {\rm GeV}/c^2$, and $O_{\rm CS} > 0.5$.

In addition to the nonresonant decay amplitude, quasi-two-body decays $B^0 \to X(\to K^0_S K^0_S) K^0_S$ via intermediate resonances X due to $b \to s$ and $b \to c$ transitions contribute to $B^0 \to K^0_S K^0_S K^0_S$ decays. We consider $b \to s$ decays to be signal, but we veto $b \to c$ contributions to measure the CP asymmetries for the $b \to s$ transition. We expect a significant $b \to c$ contribution only from $B^0 \to \chi_{c0} K^0_S$ decays based on the rates of $B^0 \to X(\to K^0_S K^0_S) K^0_S$ decays where X indicates a $\bar{D}^0, \chi_{c0}, \chi_{c1}, \chi_{c2}, \eta_c, J/\psi$, or $\psi(2S)$ meson [1]. The $B^0 \to \chi_{c0}(\to K^0_S K^0_S) K^0_S$ branching fraction is around 5% of the signal branching fraction. We reject signal B_{CP} candidates if the invariant mass of any combination of two K^0_S candidates is in the range $3.379 < M(K^0_S K^0_S) < 3.447\ {\rm GeV}/c^2$. This requirement rejects 90% of the background from $B^0 \to \chi_{c0}(\to K^0_S K^0_S) K^0_S$ decays and 7.2% of signal.

The control channel $B^+ \to K^0_S K^0_S K^+$ is reconstructed from two K^0_S mesons and a track and is similar to the signal decay. We require the particle identification information for the track to be consistent with a K^+. We use the control channel to constrain the parameters of B-vertex-resolution model for signal, as well as those of the shapes of the B_{CP} mass and $O'_{\rm CS}$ background distributions. We do not veto $\chi_{c0} K^+$ decays for the control channel because their kinematic distributions are the same as those of the $K^0_S K^0_S K^+$ final state.

IV. MEASUREMENT OF B-MESON FLAVOR AND DECAY-TIME DIFFERENCE

We use a category-based BDT algorithm to identify the $B_{\rm tag}$ flavor [23]. The algorithm uses 13 BDTs, each geared toward discriminating a specific signature of $b \to c \to s$ cascade decays using particle identification and kinematic variables of the $B_{\rm tag}$ charged decay products. The outputs from these BDTs are combined by the top-level BDT to return the flavor value q_f and tagging quality $r \equiv 1–2w$, where w is the probability for wrong flavor assignment. The probability density of Eq. (1) is modified to include the parameter w, and its difference between B^0 and $\bar{B}^0$, Δw,

$$\mathcal{P}^{\rm TD}_{\rm sig}(\Delta t, q_f) = \frac{e^{-|\Delta t|/\tau_{B^0}}}{4\tau_{B^0}} (1 - q_f \Delta w + q_f (1 - 2w)[S \sin(\Delta m_d \Delta t) - C \cos(\Delta m_d \Delta t)]). \quad (2)$$

The events are classified into seven independent r intervals (bins). For each bin, w and Δw are determined using flavor-specific B-meson decays with large branching fractions [24]. Since the signal purity varies as a function of r, using the distribution of r improves the statistical sensitivity to the CP asymmetries.

To measure Δt, we reconstruct the B_{CP} and $B_{\rm tag}$ decay vertices using information about the IP. The spatial distribution of the IP is described by a three-dimensional Gaussian whose parameters are regularly measured in a calibration based on $e^+e^- \to \mu^+\mu^-$ events. The IP size is typically 250 μm in the boost direction, 10 μm in the horizontal direction, and 0.3 μm in the vertical direction [25]. The B_{CP} vertex position is reconstructed from the six final-state pions using a decay-chain vertex fit, which constrains the B_{CP} to originate from the IP (IP constraint) [26]. Due to their long lifetime, a fraction of K^0_S mesons decay outside of the VXD volume, resulting in poorly measured decay positions. This causes the B_{CP} vertex resolution to depend strongly on the number of K^0_S mesons with associated VXD hits. In simulation, the fractions of signal decays in which zero, one, two, or three K^0_S mesons have VXD hits are 0.4%, 7.9%, 37.9%, or 53.8%, respectively. When only one K^0_S meson has VXD hits, the IP constraint significantly improves the B_{CP} vertex resolution, reducing the average vertex-position uncertainty in the boost direction from around 270 to 120 μm. The average uncertainty with the IP constraint is 49 μm when two K^0_S mesons have VXD hits and 35 μm when all three have such hits.

We use the $B_{\rm tag}$ tracks to reconstruct the $B_{\rm tag}$ vertex, excluding those having no associated PXD hits. We also exclude pairs of oppositely charged pions consistent with a K^0_S decay because they are likely to be produced away from the $B_{\rm tag}$ vertex. Similar to the B_{CP} vertex, we constrain the $B_{\rm tag}$ to originate from the IP to improve the vertex resolution and reconstruction efficiency [27]. In order to reduce the contamination from tracks from secondary and tertiary displaced vertices, which would bias the determination of the B_{CP} vertex position, the fit is repeated by iteratively removing the tracks contributing the largest increase to the vertex-fit χ^2 until a satisfactory fit quality is achieved. A selection on fit quality and vertex-position uncertainty is applied to ensure the quality of the Δt measurement.

We divide the remaining $B^0 \to K^0_S K^0_S K^0_S$ candidates into two classes based on the quality of the Δt information to maximize the sensitivity of the measurement of S and C.

For the time-differential (TD) analysis that determines both S and C, we require candidates that satisfy the following criteria: both tracks from one or more signal K_S^0 are associated with at least one VXD hit, the decay-time-difference satisfies $-30 < \Delta t < 30$ ps, satisfactory vertex-fit quality, and small vertex-position uncertainty. The Δt resolution is around 0.9 ps in the TD events. The Δt information of the other events is not used. They are included in the time-integrated (TI) analysis, which contributes only to C. The probability density in Eq. (2) is integrated over Δt for TI events, yielding

$$\mathcal{P}_{\rm sig}^{\rm TI}(q_f) = \frac{1}{2}\left(1 - q_f \Delta w - q_f(1-2w)C\frac{1}{1+\Delta m_d^2 \tau_{B^0}^2}\right). \tag{3}$$

For 1.1% of simulated signal events, multiple (typically two) B_{CP} candidates are reconstructed. We choose the candidate with the best vertex-fit quality for such events, which retains the correctly reconstructed B_{CP} candidates in 82% of these events. This requirement has negligible impact on the Δt distribution and the CP asymmetry results. The reconstruction efficiency including the $B_{\rm tag}$ selection is 28.3% in simulation. For the control channel, we reconstruct the $B^+ \to K_S^0 K_S^0 K^+$ vertex without using the K^+ track to emulate the $B^0 \to K_S^0 K_S^0 K_S^0$ vertex fit. We discard $B^+ \to K_S^0 K_S^0 K^+$ candidates that fail the TD criteria. The reconstruction efficiency for the control channel is 24.7%.

V. DETERMINATION OF SIGNAL YIELD

We extract the yields for TD, TI, and control channel events from a three-dimensional likelihood fit to the unbinned distributions of $M_{\rm bc}$, $M(K_S^0 K_S^0 K)$, where K indicates a K_S^0 or K^+ meson, and $O'_{\rm CS}$. The likelihood function includes two sample components, signal and background. We determine the shape of the signal component from fits to distributions of simulated signal and control samples. The $M_{\rm bc}$ distribution is modeled with a Gaussian function for the signal TD and control samples and with a crystal ball shape [28,29] for the signal TI sample. The signal and control-sample $M(K_S^0 K_S^0 K)$ distribution is modeled with the sum of a Gaussian function and an asymmetric Breit-Wigner function [30]. The signal and control-sample $O'_{\rm CS}$ distribution is modeled with the sum of a symmetric and an asymmetric Gaussian function [31]. For the background, the $M_{\rm bc}$ distribution is modeled with an ARGUS function [32], the $M(K_S^0 K_S^0 K)$ distribution with a linear function, and the $O'_{\rm CS}$ distribution with the sum of a symmetric and an asymmetric Gaussian function. The end point of the ARGUS function is set to $E_{\rm beam}$, which is calibrated using other B decays. The parameter sets for the $O'_{\rm CS}$ shapes are shared between TD and TI events. We use the same parameter set for the $M_{\rm bc}$ and $M(K_S^0 K_S^0 K)$ background shapes across the three samples as the $B^+ \to K_S^0 K_S^0 K^+$ kinematic properties are similar to those of the signal decay, as confirmed in simulation. The fit simultaneously determines the yield of each sample and 14 background shape parameters [33].

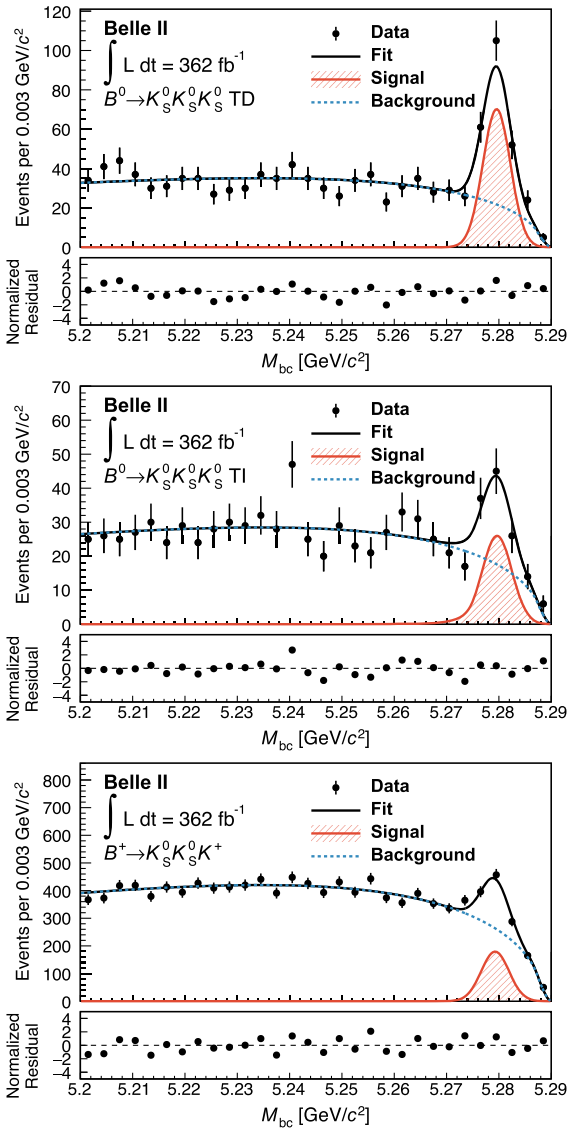

FIG. 1. Distributions of $M_{\rm bc}$ for (top) TD, (middle) TI, and (bottom) $B^+ \to K_S^0 K_S^0 K^+$ candidates with fit projections overlaid. The black dots with error bars represent the data points; the black solid curve shows the total fit projection; the red hatched area is the signal projection; and the blue dashed curve is the background projection. The distributions are restricted to events in the $M(K_S^0 K_S^0 K)$ signal region. Lower panels show the differences between data and fit results normalized by the statistical uncertainty of the data.

Figures 1–3 show the data distributions with fit results overlaid. The low-mass tails of the $M(K_S^0 K_S^0 K)$ distribution of the signal TI component is mainly due to $\pi \to \mu\nu_\mu$

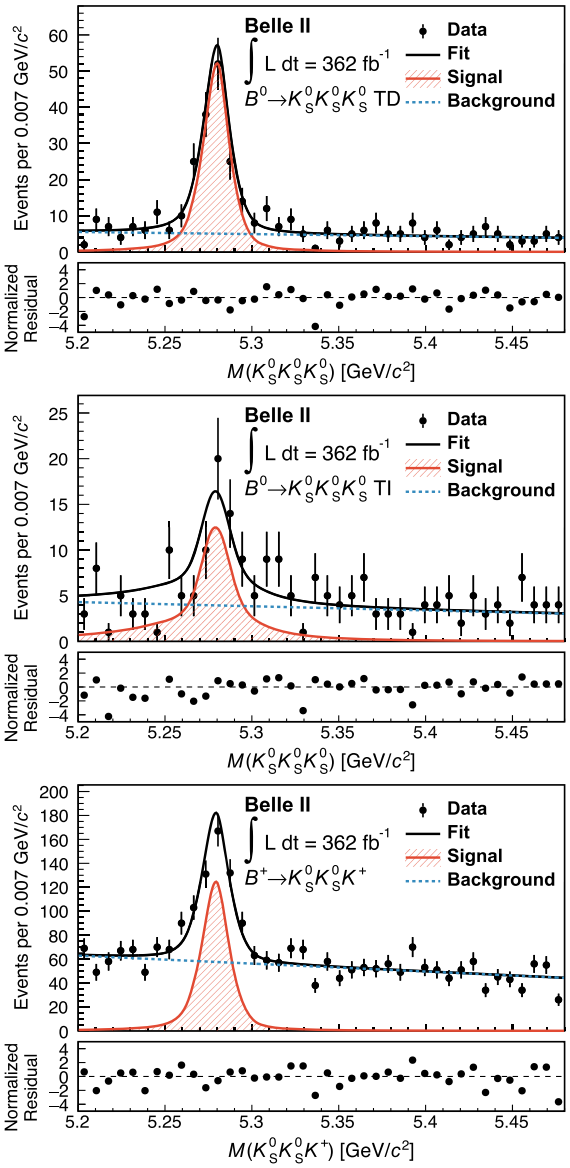

FIG. 2. Distributions of $M(K^0_S K^0_S K)$ for (top) TD, (middle) TI, and (bottom) $B^+ \to K^0_S K^0_S K^+$ candidates with fit projections overlaid. The black dots with error bars represent the data points; the black solid curve shows the total fit projection; the red hatched area is the signal projection; and the blue dashed curve is the background projection. The distributions are restricted to events in the $M_{\rm bc}$ signal region. Lower panels show the differences between data and fit results normalized by the statistical uncertainty of the data.

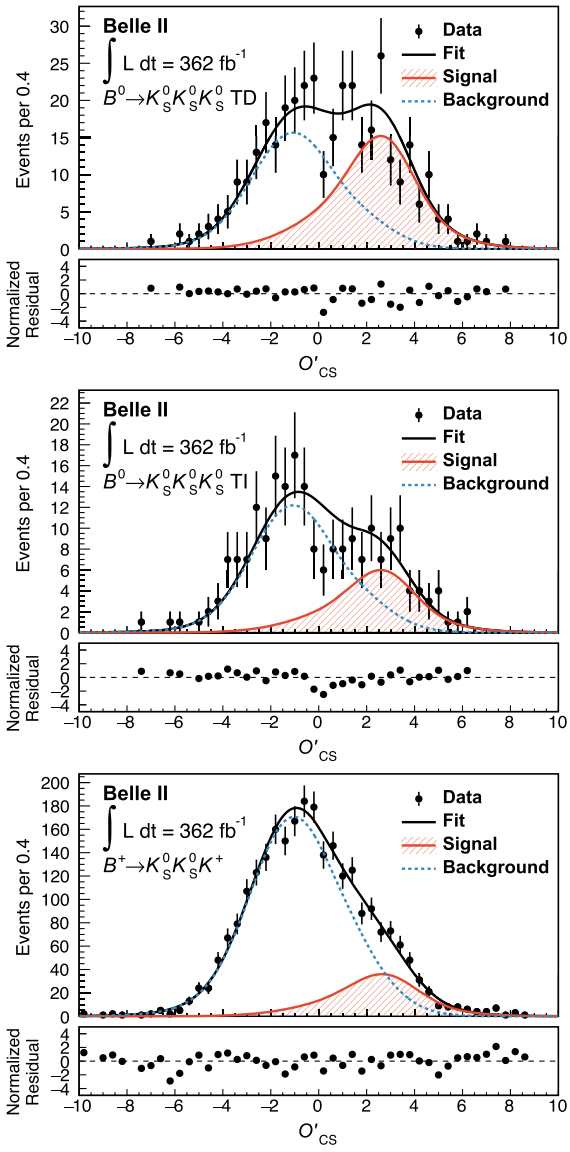

FIG. 3. Distributions of $O'_{\rm CS}$ for (top) TD, (middle) TI, and (bottom) $B^+ \to K^0_S K^0_S K^+$ candidates with fit projections overlaid. The black dots with error bars represent the data points; the black solid curve shows the total fit projection; the red hatched area is the signal projection; and the blue dashed curve is the background projection. The distributions are restricted to events in the $M_{\rm bc}$ signal region. Lower panels show the differences between data and fit results normalized by the statistical uncertainty of the data.

decays, which occur in 3% of the reconstructed signal $B^0 \to K^0_S K^0_S K^0_S$ events. Such events are mostly classified as TI events due to the poor vertex-fit quality. We define the signal region as $5.272 < M_{\rm bc} < 5.288\,{\rm GeV}/c^2$, $5.2 < M(K^0_S K^0_S K) < 5.36\ {\rm GeV}/c^2$, and $-4.44 < O'_{\rm CS} < 8.85$. Each range for $M_{\rm bc}$ and $O'_{\rm CS}$ retains 99.73% of signal TD events. The signal yield and the purity in the signal region is 158^{+14}_{-13} and 57% for TD events, 62 ± 9 and 40% for TI events, and 403^{+24}_{-23} and 22% for the control channel events.

VI. DETERMINATION OF *CP* ASYMMETRIES

We determine the *CP* asymmetries S and C from a maximum-likelihood fit to the unbinned Δt and binned q_f distributions combining TD, TI, and $B^+ \to K^0_S K^0_S K^+$ events restricted to the signal region. The contribution to the likelihood function from the ith TD event is

$$\mathcal{L}_i^{\mathrm{TD}}(S, C|\Delta t_i, q_{f,i}) = f_i^{\mathrm{sig}} \int d(\Delta t') R(\Delta t_i - \Delta t') \mathcal{P}_{\mathrm{sig}}^{\mathrm{TD}}(\Delta t', q_{f,i}) + (1 - f_i^{\mathrm{sig}}) \mathcal{P}_{\mathrm{bkg}}(\Delta t_i), \quad (4)$$

where $R(\Delta t_i - \Delta t')$ is the response function of the Δt measurement (resolution function), f_i^{sig} is the signal probability of the ith event, and $\mathcal{P}_{\mathrm{bkg}}$ is the Δt distribution of background events. We use a resolution function developed by the Belle Collaboration [34]. The resolution function is the convolution of four components: detector resolution for the B_{CP} vertex, detector resolution for the B_{tag} vertex, bias due to secondary particles from charmed intermediate states for the B_{tag} vertex, and corrections to the boost factor due to the nonzero c.m. momentum of the B mesons. The correction to the boost factor is calculated analytically using the cosine of the angle between the B_{CP} momentum and the boost direction in the e^+e^- c.m. frame, $\cos\theta_B^*$, on an event-by-event basis. The resolution-function parameters are fixed to those obtained from a fit to simulated signal events, but the width in simulation is scaled by a parameter s_{det} that accounts for data-simulation differences and that is determined simultaneously with S and C. The distribution $\mathcal{P}_{\mathrm{bkg}}$ is the sum of two Gaussian functions that depend on vertex quality and vertex-position uncertainty. The $\mathcal{P}_{\mathrm{bkg}}$ parameters are determined by a fit to the M_{bc} sideband data. The likelihood function assumes equal fraction of B^0-tagged and $\bar{B}^0$-tagged background events as confirmed in the sideband data and in the simulation. We calculate the signal probability on an event-by-event basis using the five-dimensional PDF of M_{bc}, $M(K_S^0K_S^0K)$, O'_{CS}, r, and $\cos\theta_B^*$. The PDF contains signal and background components, whose fractions are determined by the signal and background yields. No correlation is assumed between the variables. The last two variables are included to avoid fit biases (0.03 for S and 0.02 for C) due to implicitly assuming equal distributions that differ across sample components [35]. The r distribution for background is obtained from the $M_{\mathrm{bc}} < 5.265\ \mathrm{GeV}/c^2$ sideband. For $\cos\theta_B^*$, we assume a uniform distribution for background and $\frac{3}{4}(1 - \cos^2\theta_B^*)$ for signal. For TI events, we use the likelihood in Eq. (4) integrated over Δt,

$$\mathcal{L}_i^{\mathrm{TI}}(C|q_{f,i}) = f_i^{\mathrm{sig}} \mathcal{P}_{\mathrm{sig}}^{\mathrm{TI}}(q_{f,i}) + \frac{1 - f_i^{\mathrm{sig}}}{2}. \quad (5)$$

We include the $B^+ \to K_S^0K_S^0K^+$ decays in the fit using the likelihood in Eq. (4) summed over q_f and using the B^+ lifetime instead of the B^0 lifetime. The control channel helps to constrain s_{det} since its signal yield is 2.5 times larger than the TD signal. The resolution-function parameters and s_{det} are the same as those of the $B^0 \to K_S^0K_S^0K_S^0$ events except for the parameters that model the effect of secondary particles. They differ since, compared to B^0 mesons, B^+ mesons yield fewer D^- mesons and more $\bar{D}^0$ mesons, which have shorter lifetimes. We define the background Δt distribution for $B^+ \to K_S^0K_S^0K^+$ with an independent parameter set from $B^0 \to K_S^0K_S^0K_S^0$ and with an additional Gaussian function.

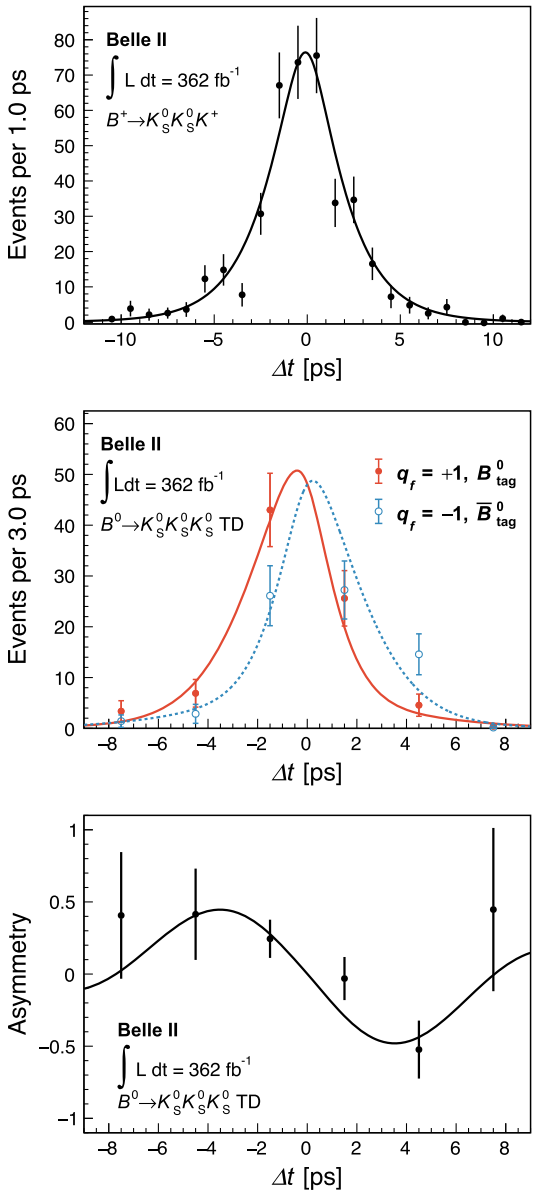

FIG. 4. Background-subtracted Δt distributions for (top) $B^+ \to K_S^0K_S^0K^+$ candidates and (middle) $B^0 \to K_S^0K_S^0K_S^0$ TD candidates separated for $q_f = \pm 1$ along with (bottom) the resulting B^0_{tag} minus $\bar{B}^0_{\mathrm{tag}}$ yield asymmetry as a function of Δt. Points with error bars represent data and the curves show the fit results. Red, filled circles and solid curves show the data for $q_f = +1$ and fit results, respectively, while blue, open circles and dashed curves are for $q_f = -1$.

Figure 4 shows the background-subtracted Δt distributions using the ${}_s\mathcal{P}lot$ technique [36] and their asymmetry with fit projections overlaid. We obtain $S = -1.37^{+0.32}_{-0.26}$,

$C = -0.07 \pm 0.17$, and $s_{\rm det} = 1.16 \pm 0.15$. Linear correlation coefficients are -0.02 between S and C, -0.16 between S and $s_{\rm det}$, and -0.07 between C and $s_{\rm det}$. However, simulation studies show that the above point estimates are not reliable. While the likelihood has no secondary maxima, the small sample size leads to biases and non-Gaussian uncertainties. For more reliable results, we construct confidence regions for the CP-violating parameters as described in Sec. VIII.

VII. SYSTEMATIC UNCERTAINTIES

We consider various sources of systematic uncertainties, which are listed in Table I. To evaluate the systematic uncertainties in S and C related to assumptions made on parameters of the fit model, we repeat the fit on data using alternative values of the parameters sampled from Gaussian distributions based on their uncertainties. The widths of the resulting distributions of S and C are taken as contributions to the systematic uncertainty. This approach is used for τ_{B^0}, τ_{B^+}, and Δm_d; the parameters of the $M_{\rm bc}$, $M(K^0_S K^0_S K)$, and $O'_{\rm CS}$ shapes (referred to as signal modeling in the table); the parameters describing the resolution function; the parameters for the background Δt shape; and the parameters related to flavor tagging.

We sample the world averages of the B^0 and B^+ lifetimes and Δm_d including their uncertainties [1]. The parameters of signal probability, resolution function, and background Δt shape have uncertainties from the fits used to determine them, which depend on the size of data and simulated samples. The systematic uncertainty in the resolution function includes the uncertainty due to the choice of the model, which is determined by analyzing a simulated sample with alternative resolution models whose dependence on the vertex-fit quality is partly or entirely removed. The simulation assumes $S = -0.7$ and $C = 0$. The systematic uncertainty due to flavor tagging takes into account the statistical and systematic uncertainties of w and Δw. It also includes the bias due to the flavor asymmetry in the tagging efficiency between B^0 and $\bar{B}^0$. Two sets of simplified simulated experiments are generated, with and without the asymmetry, and fits for S and C are performed in both ignoring the asymmetry. The difference between the mean values of S and C obtained in the two sets is the uncertainty. We repeat the simplified simulation assuming various input CP asymmetries and take the maximum difference. We observe correlations between $M(K^0_S K^0_S K)$ and vertex-fit quality for B_{CP} (-0.06 for TD events), and between $O'_{\rm CS}$ and r (0.15), which are not included in the default model. To evaluate the bias due to these correlations and to a mismodeling of the $\cos\theta^*_B$ distribution, we use simplified simulated samples generated with and without these effects in the same way as above. The CP asymmetries are affected by the interference between a CKM-favored transition $\bar{b} \to \bar{c}u\bar{d}$ and a doubly CKM-suppressed transition $b \to u\bar{c}d$ on the tag side [37]. We assign as a systematic uncertainty the effect of the tag-side interference assuming $S = -0.7$ and $C = 0$. The systematic uncertainty due to the vertex reconstruction is determined by varying the parameters describing the IP profile and boost vector, the track requirements used in the $B_{\rm tag}$ vertex reconstruction, and the criteria to select TD events, and repeating the fit on data. To evaluate the effect from possible misalignment of the vertex detector, we use four simulated samples, each assuming a different misalignment configuration and CP asymmetries of $S = -1.0$ and $C = 0$. We compare the resulting CP asymmetries with those in the sample without misalignment and the maximum deviation is taken as the systematic uncertainty.

TABLE I. Systematic uncertainties.

Source	S	C
τ_{B^0}, τ_{B^+}, and Δm_d	0.009	0.000
Signal modeling	0.014	0.008
Δt resolution function	0.013	0.008
Background Δt modeling	0.004	0.002
Flavor tagging	0.013	0.012
Fit bias	0.014	0.004
Tag-side interference	0.001	0.027
Vertex reconstruction	0.011	0.004
Tracker misalignment	0.008	0.007
Total	0.030	0.033

VIII. RESULTS AND SUMMARY

Since the point estimates from the fit are not reliable, we construct confidence regions for our results based on likelihood-ratio ordering [38]. For the construction, simplified simulated experiments are generated by sampling the likelihoods of the yield fit and asymmetry fit. The nuisance parameters in the models are fixed to the values fitted to the data and the systematic uncertainty is not taken into account as its size is negligible. Figure 5 shows the resulting two-dimensional confidence regions where S and C are constrained within their physical boundary, $S^2 + C^2 \leq 1$. The projections of the confidence regions are $-1 < S < -0.72$ and $-0.29 < C < 0.14$ at the 68.3% confidence level, $-1 < S < -0.41$ and $-0.45 < C < 0.32$ at the 95.5% confidence level, and $-1 < S < -0.09$ and $-0.61 < C < 0.49$ at the 99.7% confidence level. The results are consistent with the SM predictions and current best determinations by the Belle and *BABAR* experiments [9–11].

In summary, we report a measurement of decay-time-dependent CP asymmetries in $B^0 \to K^0_S K^0_S K^0_S$ decays using a dataset of 387×10^6 $B\bar{B}$ pairs reconstructed from electron-positron collisions at the $\Upsilon(4S)$ and collected with Belle II experiment from 2019 to 2022. We reconstruct 220 signal events and extract the CP-violating parameters

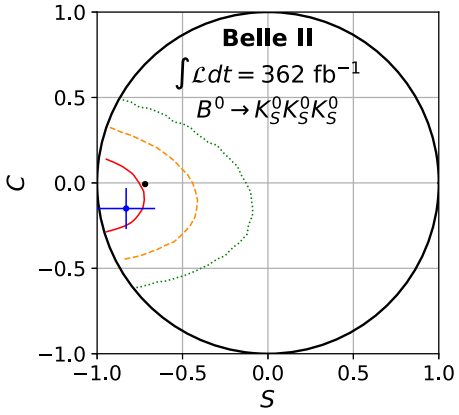

FIG. 5. Two-dimensional confidence regions for S and C based on likelihood-ratio ordering. The red solid, orange dashed, and green dotted contours represent the 68.27%, 95.45%, and 99.73% confidence regions for S and C given the physical constraint $S^2 + C^2 \leq 1$. The blue dot with the error bar is the average value based on results by Belle and *BABAR* [9,10]. The black dot represents the SM prediction $(S, C) = (-\sin 2\phi_1 - 0.02, -0.007)$ based on measurements in $B^0 \to (c\bar{c})K^0$ decays [11].

from a fit to the distribution of the decay-time difference of the two B mesons. We determine a two-dimensional confidence region for the relevant parameters S and C obtaining results that are consistent with the SM predictions and previous determinations.

The Belle II analysis software framework used in this paper is openly available from the Zenodo repository [21].

ACKNOWLEDGMENTS

This work, based on data collected using the Belle II detector, was supported by Higher Education and Science Committee of the Republic of Armenia Grant No. 23LCG-1C011; Australian Research Council and Research Grants No. DP200101792, No. DP210101900, No. DP210102831, No. DE220100462, No. LE210100098, and No. LE230100085; Austrian Federal Ministry of Education, Science and Research, Austrian Science Fund No. P 31361-N36 and No. J4625-N, and Horizon 2020 ERC Starting Grant No. 947006 "InterLeptons"; Natural Sciences and Engineering Research Council of Canada, Compute Canada, and CANARIE; National Key R&D Program of China under Contract No. 2022YFA1601903, National Natural Science Foundation of China and Research Grants No. 11575017, No. 11761141009, No. 11705209, No. 11975076, No. 12135005, No. 12150004, No. 12161141008, and No. 12175041, and Shandong Provincial Natural Science Foundation Project ZR2022JQ02; the Czech Science Foundation Grant No. 22-18469S; European Research Council, Seventh Framework PIEF-GA-2013-622527, Horizon 2020 ERC-Advanced Grants No. 267104 and No. 884719, Horizon 2020 ERC-Consolidator Grant No. 819127, Horizon 2020 Marie Sklodowska-Curie Grant Agreement No. 700525 "NIOBE" and No. 101026516, and Horizon 2020 Marie Sklodowska-Curie RISE project JENNIFER2 Grant Agreement No. 822070 (European grants); L'Institut National de Physique Nucléaire et de Physique des Particules (IN2P3) du CNRS and L'Agence Nationale de la Recherche (ANR) under grant ANR-21-CE31-0009 (France); BMBF, DFG, HGF, MPG, and AvH Foundation (Germany); Department of Atomic Energy under Project Identification No. RTI 4002, Department of Science and Technology, and UPES SEED funding programs No. UPES/R&D-SEED-INFRA/17052023/01 and No. UPES/R&D-SOE/20062022/06 (India); Israel Science Foundation Grant No. 2476/17, U.S.-Israel Binational Science Foundation Grant No. 2016113, and Israel Ministry of Science Grant No. 3-16543; Istituto Nazionale di Fisica Nucleare and the Research Grants BELLE2; Japan Society for the Promotion of Science, Grant-in-Aid for Scientific Research Grants No. 16H03968, No. 16H03993, No. 16H06492, No. 16K05323, No. 17H01133, No. 17H05405, No. 18K03621, No. 18H03710, No. 18H05226, No. 19H00682, No. 20H05850, No. 20H05858, No. 22H00144, No. 22K14056, No. 22K21347, No. 23H05433, No. 26220706, and No. 26400255, the National Institute of Informatics, and Science Information NETwork 5 (SINET5), and the Ministry of Education, Culture, Sports, Science, and Technology (MEXT) of Japan; National Research Foundation (NRF) of Korea Grants No. 2016R1D1A1B02012900, No. 2018R1A2B3003643, No. 2018R1A6A1A06024970, No. 2019R1I1A3A01058933, No. 2021R1A6A1A03043957, No. 2021R1F1A1060423, No. 2021R1F1A1064008, No. 2022R1A2C1003993, and No. RS-2022-00197659, Radiation Science Research Institute, Foreign Large-Size Research Facility Application Supporting project, the Global Science Experimental Data Hub Center of the Korea Institute of Science and Technology Information and KREONET/GLORIAD; Universiti Malaya RU grant, Akademi Sains Malaysia, and Ministry of Education Malaysia; Frontiers of Science Program Contracts No. FOINS-296, No. CB-221329, No. CB-236394, No. CB-254409, and No. CB-180023, and SEP-CINVESTAV Research Grant No. 237 (Mexico); the Polish Ministry of Science and Higher Education and the National Science Center; the Ministry of Science and Higher Education of the Russian Federation and the HSE University Basic Research Program, Moscow; University of Tabuk Research Grants No. S-0256-1438 and No. S-0280-1439 (Saudi Arabia); Slovenian Research Agency and Research Grants No. J1-9124 and No. P1-0135; Agencia Estatal de Investigacion, Spain Grant No. RYC2020-029875-I and Generalitat Valenciana, Spain Grant No. CIDEGENT/2018/020; National Science and Technology Council, and Ministry of Education

(Taiwan); Thailand Center of Excellence in Physics; TUBITAK ULAKBIM (Turkey); National Research Foundation of Ukraine, Project No. 2020.02/0257, and Ministry of Education and Science of Ukraine; the U.S. National Science Foundation and Research Grants No. PHY-1913789 and No. PHY-2111604, and the U.S. Department of Energy and Research Awards No. DE-AC06-76RLO1830, No. DE-SC0007983, No. DE-SC0009824, No. DE-SC0009973, No. DE-SC0010007, No. DE-SC0010073, No. DE-SC0010118, No. DE-SC0010504, No. DE-SC0011784, No. DE-SC0012704, No. DE-SC0019230, No. DE-SC0021274, No. DE-SC0021616, No. DE-SC0022350, No. DE-SC0023470; and the Vietnam Academy of Science and Technology (VAST) under Grants No. NVCC.05.12/22-23 and No. DL0000.02/24-25. We thank the SuperKEKB team for delivering high-luminosity collisions; the KEK cryogenics group for the efficient operation of the detector solenoid magnet; the KEK computer group and the NII for on-site computing support and SINET6 network support; and the raw-data centers at BNL, DESY, GridKa, IN2P3, INFN, and the University of Victoria for off-site computing support.

These acknowledgements are not to be interpreted as an endorsement of any statement made by any of our institutes, funding agencies, governments, or their representatives.

[1] R. L. Workman *et al.* (Particle Data Group), Prog. Theor. Exp. Phys. **2022**, 083C01 (2022).
[2] Y. Grossman and M. P. Worah, Phys. Lett. B **395**, 241 (1997).
[3] M. Kobayashi and T. Maskawa, Prog. Theor. Phys. **49**, 652 (1973).
[4] A. B. Carter and A. I. Sanda, Phys. Rev. Lett. **45**, 952 (1980).
[5] A. B. Carter and A. I. Sanda, Phys. Rev. D **23**, 1567 (1981).
[6] I. I. Y. Bigi and A. I. Sanda, Nucl. Phys. **B193**, 85 (1981).
[7] The coefficients (S, C) are written $(S, -A)$ elsewhere.
[8] H. Y. Cheng, C. K. Chua, and A. Soni, Phys. Rev. D **72**, 094003 (2005).
[9] K. H. Kang *et al.* (Belle Collaboration), Phys. Rev. D **103**, 032003 (2021).
[10] J. P. Lees *et al.* (*BABAR* Collaboration), Phys. Rev. D **85**, 054023 (2012).
[11] Y. S. Amhis *et al.* (HFLAV Collaboration), Phys. Rev. D **107**, 052008 (2023).
[12] K. Akai, K. Furukawa, and H. Koiso (SuperKEKB Collaboration), Nucl. Instrum. Methods Phys. Res., Sect. A **907**, 188 (2018).
[13] T. Abe *et al.* (Belle II Collaboration), arXiv:1011.0352.
[14] K. Adamczyk *et al.* (Belle II SVD Collaboration), J. Instrum. **17**, P11042 (2022).
[15] D. Kotchetkov *et al.*, Nucl. Instrum. Methods Phys. Res., Sect. A **941**, 162342 (2019).
[16] D. J. Lange, Nucl. Instrum. Methods Phys. Res., Sect. A **462**, 152 (2001).
[17] T. Sjöstrand, S. Ask, J. R. Christiansen, R. Corke, N. Desai, P. Ilten, S. Mrenna, S. Prestel, C. O. Rasmussen, and P. Z. Skands, Comput. Phys. Commun. **191**, 159 (2015).
[18] S. Jadach, B. F. L. Ward, and Z. Was, Comput. Phys. Commun. **130**, 260 (2000).
[19] S. Agostinelli *et al.*, Nucl. Instrum. Methods Phys. Res., Sect. A **506**, 250 (2003).
[20] T. Kuhr, C. Pulvermacher, M. Ritter, T. Hauth, and N. Braun (Belle II Framework Software Group), Comput. Software Big Sci. **3**, 1 (2019).
[21] Belle II Collaboration, Belle II analysis software framework (basf2) Zenodo, 10.5281/zenodo.6949513 (2022).
[22] S. H. Lee *et al.* (Belle Collaboration), Phys. Rev. Lett. **91**, 261801 (2003).
[23] F. Abudinén *et al.* (Belle II Collaboration), Eur. Phys. J. C **82**, 283 (2022).
[24] I. Adachi *et al.* (Belle II Collaboration), arXiv:2302.12898.
[25] F. J. Abudinen *et al.* (Belle II Collaboration), Phys. Rev. D **107**, L031103 (2023).
[26] J. F. Krohn *et al.* (Belle II Analysis Software Group), Nucl. Instrum. Methods Phys. Res., Sect. A **976**, 164269 (2020).
[27] S. Dey and A. Soffer, Springer Proc. Phys. **248**, 411 (2020).
[28] J. Gaiser, Charmonium spectroscopy from radiative decays of the J/ψ and ψ', Ph.D. thesis, Stanford University, 1982.
[29] T. Skwarnicki, A study of the radiative CASCADE transitions between the Upsilon-Prime and Upsilon resonances, Ph.D. thesis, Cracow, INP, 1986.
[30] We define an asymmetric Breit-Wigner function as

$$f(x;\mu,\gamma_L,\gamma_R) = \frac{1}{\pi\bar{\gamma}(1+\frac{(x-\mu)^2}{\gamma^2})},$$

where $\bar{\gamma} = (\gamma_L + \gamma_R)/2$ and $\gamma = \gamma_{L(R)}$ at $x < (\geq)\mu$.
[31] We define an asymmetric Gaussian function as

$$g(x;\mu,\sigma_L,\sigma_R) = \frac{1}{\sqrt{2\pi}\bar{\sigma}} e^{-\frac{(x-\mu)^2}{2\sigma^2}},$$

where $\bar{\sigma} = (\sigma_L + \sigma_R)/2$ and $\sigma = \sigma_{L(R)}$ at $x < (\geq)\mu$.
[32] H. Albrecht *et al.* (ARGUS Collaboration), Phys. Lett. B **241**, 278 (1990).
[33] F. James and M. Roos, Comput. Phys. Commun. **10**, 343 (1975).

[34] H. Tajima *et al.*, Nucl. Instrum. Methods Phys. Res., Sect. A **533**, 370 (2004).
[35] G. Punzi, arXiv:physics/0401045.
[36] M. Pivk and F. R. Le Diberder, Nucl. Instrum. Methods Phys. Res., Sect. A **555**, 356 (2005).
[37] O. Long, M. Baak, R. N. Cahn, and D. P. Kirkby, Phys. Rev. D **68**, 034010 (2003).
[38] G. J. Feldman and R. D. Cousins, Phys. Rev. D **57**, 3873 (1998).